

Received August 31, 2019, accepted October 8, 2019, date of publication October 22, 2019, date of current version November 22, 2019.

Digital Object Identifier 10.1109/ACCESS.2019.2949017

Embedding a Rydberg Atom-Based Sensor Into an Antenna for Phase and Amplitude Detection of Radio-Frequency Fields and Modulated Signals

MATTHEW T. SIMONS, (Member, IEEE), ABDULAZIZ H. HADDAB^{ID}, (Student Member, IEEE), JOSHUA A. GORDON^{ID}, (Senior Member, IEEE), DAVID NOVOTNY, AND CHRISTOPHER L. HOLLOWAY^{ID}, (Fellow, IEEE)

National Institute of Standards and Technology (NIST), Boulder, CO 80305, USA

Corresponding author: Christopher L. Holloway (holloway@boulder.nist.gov)

ABSTRACT We demonstrate a Rydberg atom-based sensor embedded in a parallel-plate waveguide (PPWG) for amplitude and phase detection of a radio-frequency (RF) electric field. This embedded atomic sensor is also capable of receiving modulated communications signals. In this configuration, the PPWG antenna serves two functions. First, the PPWG antenna acts as a source for a local oscillator (LO) field. The LO is required to use an atomic vapor cell (a glass cell containing a Rydberg atom vapor) as a Rydberg atom-based mixer, which detects the amplitude and phase of a second RF field incident from some remote location. The second function of the PPWG antenna is to capture the RF field arriving from a remote location and concentrate it at the location of the atomic vapor cell for detection. To demonstrate this, we show several examples of phase and amplitude measurements of an RF field with the embedded Rydberg-atom sensor. We also demonstrate the discrimination of the polarization of an RF field and the ability to receive phase-modulated carrier communications signals with this integrated atomic sensor. Embedding the atomic sensor in an antenna allows for the full characterization of a radio frequency field, in that the magnitude, phase, and polarization of an RF field can be measured with one compact integrated quantum-based sensor. Furthermore, the embedded sensor head allows one to easily vary the LO in order to maximize the ability to measure phase and amplitude of the field or modulated signal.

INDEX TERMS Atom-based antenna, atom-based receiver, amplitude detection, embedded sensor, phase detection, modulated signal detection, atomic physics, electromagnetically induced transparency (EIT), Rydberg atoms, quantum optics, quantum-based metrology.

I. INTRODUCTION

There is a rapidly growing interest in the potential applications of Rydberg atom-based sensors. These type of sensors can replace the front-end components and electronics in a conventional antenna/receiver system, and as such, they have potential advantages over conventional systems. The purpose of this paper is to demonstrate the integration of atomic vapor cells with waveguiding structures for the development of compact Rydberg atom-based sensors/receivers.

Rydberg atoms have one or more electrons excited to a very high principal quantum number n [1], which have many useful properties that scale with n . For example, their large dipole moments (scale as n^2) make the atoms sensitive to electric (E)

fields, which make them useful for E-field sensors. The re-definition of the International System of Units (SI) that occurred in November of 2018 made it possible to make direct SI-traceable measurements for E-fields using Rydberg atoms. The basic idea uses a technique known as electromagnetically induced transparency (EIT) and Autler-Townes (AT) splitting to detect a radio-frequency (RF) E-field, where the E-field is shown to be directly proportional to Planck's constant, which is exactly defined in the re-definition of the SI [2] and [3].

The idea of developing a fundamentally new method for measuring RF E-fields with Rydberg atoms started about eight years ago when two groups (one led by the University of Oklahoma and one led by the National Institute of Standards and Technology) launched sizable efforts to investigate the feasibility of using Rydberg atoms for SI-traceable E-field strength measurements [4], [5], and [6]. Since this time,

The associate editor coordinating the review of this manuscript and approving it for publication was Sandra Costanzo^{ID}.

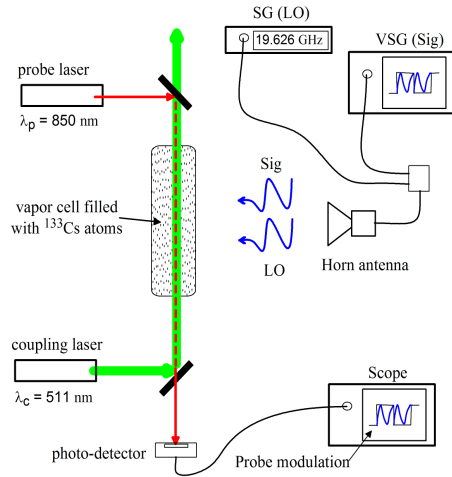


FIGURE 1. Diagram of one of the original implementations of the Rydberg atom-based mixer [29].

much progress has been made in the use of Rydberg atom-based E-field sensors by various groups [7]–[24]. Most of this work concentrated on the amplitude (both weak and strong field strengths) and polarization. However, recently we developed a technique that allows for the detection of RF phase (a Rydberg atom-based mixer) [25]. While a Rydberg atom-based mixer for phase measurements was introduced in [25], its implementation was not the most convenient due to the location of a reference field (discussed in detail below). In this paper, we demonstrate that by placing an atomic-vapor cell inside a parallel-plate waveguide (PPWG) antenna, it serves as a receiver for detecting the phase and amplitude of RF E-field and phase-modulated signals. This embedded atomic-vapor cell allows for the full characterization of an RF field and a modulated signal in one compact sensor, i.e., the integrated sensor can measure amplitude, phase, and polarization.

Fig. 1 shows a diagram of one of the original implementations of the Rydberg atom-based mixer. It allows for the detection of amplitude and phase of weak E-fields with sub-Hz frequency resolution. A probe laser is passed through a vapor cell. A second coupling laser establishes coherence between the atomic states, enhancing the probe transmission. This process is called EIT. This transmission is further altered in the presence of an applied RF field. In the Rydberg-atom mixer scheme, two RF fields are involved, a reference field (labeled as “LO”) and the field or signal of interest (labeled as “SIG”). The reference RF field at frequency f_{LO} , on-resonance with a Rydberg atomic transition, acts as a local oscillator (LO). Then, the presence of a signal field (SIG) at frequency f_{SIG} creates a beat note in the probe laser transmission, whose amplitude varies as [25]

$$T \propto \cos(2\pi f_{IF}t + \Delta\phi), \tag{1}$$

where $\Delta\phi$ is the phase difference between the LO and SIG fields and f_{IF} is the frequency of the beat note, given by

$$f_{IF} = f_{SIG} \pm f_{LO}. \tag{2}$$

The read-out of the phase of the SIG is performed by monitoring the transmission of a probe laser through the vapor cell. This beat note formed from the LO and SIG fields results in amplitude modulation (AM) of the probe transmission. This AM of the probe laser transmission can be detected with a photodetector and used to determine the phase of the SIG. For a phase modulated carrier, the Rydberg atoms automatically down-convert the carrier to the IF, which contains the phase of the SIG. In effect, the atoms are acting as a down-conversion mixer. The Rydberg atom-based mixer can also be used to detect weak fields with sub-Hz frequency resolution [28].

While the configuration in Fig. 1 is for the case where both the LO and SIG are applied via the same horn [29], the LO and SIG can also be applied with two different horns [25]. The problem with both these configurations is that they require the LO to be transmitted alongside the SIG. There are several situations where this is not possible, that is, one may not always be able to have an LO at the same location as the source of the SIG. An example would be trying to receive a transmitted signal (the SIG) from a remote location. However, by embedding the vapor cell into a receive antenna (e.g., a PPWG antenna), the receiving antenna can apply the LO while capturing the SIG from a remote location. The embedded sensor allows one to easily vary the LO in order to maximize the beat note signal strength and hence maximize the ability to measure phase and amplitude of the SIG. In this paper, we demonstrate such an embedded atomic sensor and show various results to illustrate its capabilities.

In the original development of this Rydberg atom-based approach, the goal was to develop a quantum direct SI-traceable measurement of an RF E-field, which results in a calibrated, absolute measurement of the E-field strength. However, the Rydberg-atom approach has other applications, including use as a sensor for relative field strength measurements or as a receiver. In these types of applications, absolute measurements of a field are not required. The embedded sensor discussed in this paper is intended for these non-absolute measurements. The presence of the metal PPWG structure perturbs the field being measured, which diminishes the applicability for absolute E-field strength measurements. On the other hand, the PPWG enhances the ability for the embedded sensor to be used as a receiver and/or as a device for phase-sensitive detection.

Vapor cells embedded into metallic structures have been demonstrated in the past for different applications [15] and [30]. In [15] it is demonstrated that embedding a vapor cell into a passive metallic structure can aid in field enhancement and polarization selectivity. The results of our work illustrate how embedding vapor cell into a metallic structure allows for a convenient method to apply an LO for phase detection and other applications.

II. EMBEDDED VAPOR CELL

Fig. 2 shows a photo of the embedded atom-based sensor. It consists of a 4 mm by 8 mm by 10 mm rectangular vapor cell filled with cesium (^{133}Cs) atoms. The vapor cell is embedded

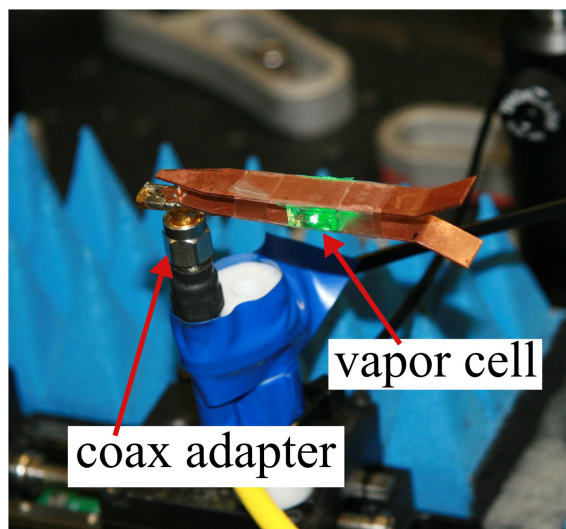


FIGURE 2. Sensor head: a vapor cell embedded into a PPWG antenna. The green coupling laser propagating through the vapor cell can be seen in the photo. The LO is supplied by the coaxial input, and the SIG is coupled through the flared end.

into a PPWG antenna. The PPWG antenna has a length of 50 mm, a plate separation of 4 mm, and width of 8 mm. The antenna is flared (flare length of 10 mm and flare angle of 30°) at one end for impedance matching. The other end of the antenna is connected to a coaxial adapter. A continuous wave (CW) field is injected into the antenna via the coaxial adapter, which serves as the LO for the sensor head. The flared end of the antenna is pointed toward the incoming signal to be detected.

The vapor cell is held in place with transparent tape. One can also use epoxy for a more rugged design (similar to that done in [23]). As long as care is used in the application of the adhesive (either the tape and/or epoxy), the adhesive method will have minimal effects on the performance of the sensor for the applications discussed in this paper.

The presence of the dielectric walls of the vapor cell causes internal resonance (or standing waves) of the RF field inside the vapor cell [7], [8], [31], and [32]. These standing waves can affect the ability to perform calibrated, absolute measurements of the E-field strength. However, if the position of the lasers in the vapor cell is fixed, the standing waves will not affect the ability to perform relative field strength measurements or the ability to detect the phase of the field. The internal resonances do not affect the types of experiments performed in this paper.

Compared with other work in the literature, where the main focus was on RF field amplitude measurements, this work demonstrates a Rydberg atom-based sensor capable of simultaneously measuring amplitude and phase, along with polarization selectivity. The atomic-vapor cell could also be embedded in various other types of antenna and waveguiding structures for a wide array of applications ranging from polarization selectivity to weak field detection.

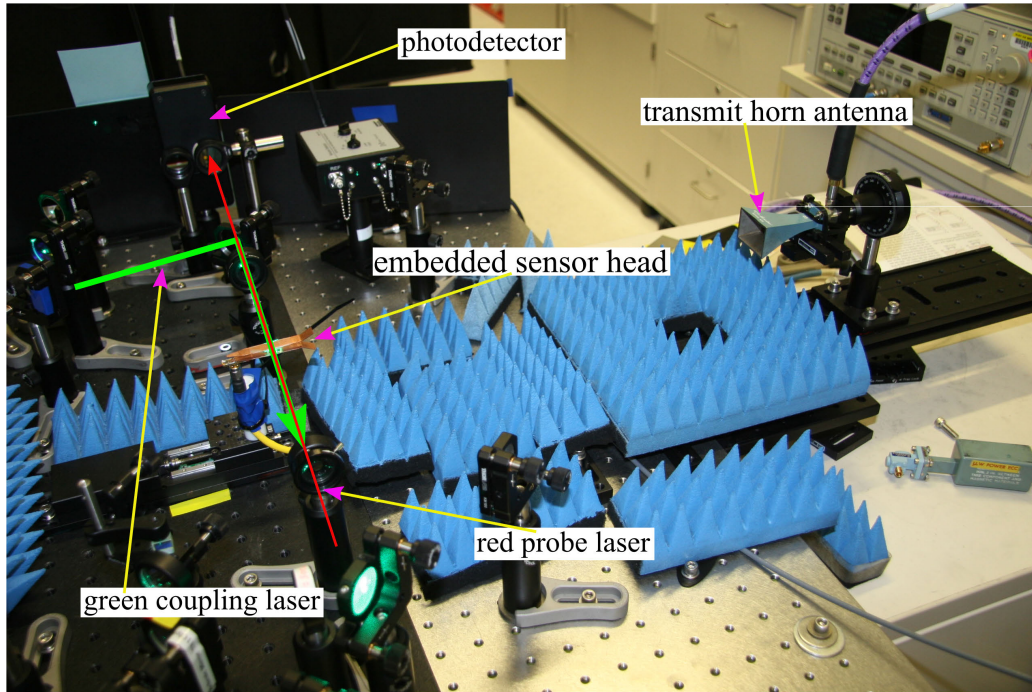
III. EXPERIMENTAL SETUP

A photo and diagram of the experimental setup is shown in Fig. 3, which consists of an 850 nm probe laser, a 511 nm coupling laser, a photo detector, oscilloscope, transmitting horn antenna, and the embedded sensor head (the PPWG antenna with the embedded vapor cell filled with ^{133}Cs atoms). The horn antenna is used to transmit a signal to be detected by the embedded sensor. A signal generator (SG) is used to apply the LO into the PPWG antenna. To generate the SIG field we use a vector signal generator (VSG) connected to the horn antenna. The VSG can supply a CW carrier or various types of digital modulation schemes (amplitude-modulation (AM) and/or phase modulation of a CW carrier). The frequency of the CW SIG field is given in (2), where f_{LO} and f_{IF} are changed during these experiments. An RF isolator is placed between the embedded sensor head and the SG in order to isolate and protect the SG from any energy received from the SIG source.

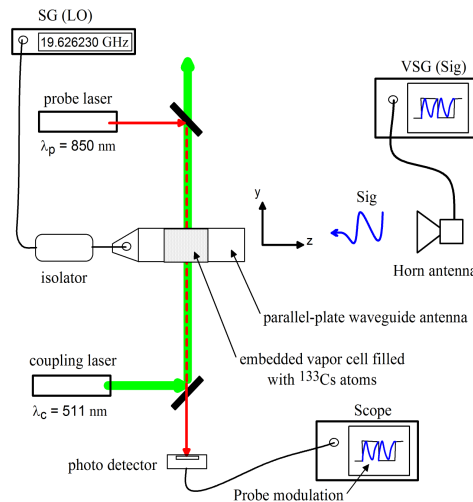
The probe laser is locked to the D_2 transition (or wavelength of $\lambda_p = 852.347$ nm [33]) for ^{133}Cs (corresponding to atomic states $6S_{1/2}$ - $6P_{3/2}$) and focused to a full-width at half maximum (FWHM) of $425 \mu\text{m}$, with different powers level depending on the experiments. To produce an EIT signal, we couple to the ^{133}Cs $6P_{3/2}$ - $34D_{5/2}$ states by applying a counter-propagating coupling laser at $\lambda_c = 511.148$ nm (focused to a FWHM of $620 \mu\text{m}$). The LO field (around 19.629 GHz) couples the Rydberg states $34D_{5/2}$ and $35P_{3/2}$. The output of the photodetector is connected to an oscilloscope. The beat note is displayed on the oscilloscope and the phase change of the SIG can be determined by the phase change of the beat note.

While we use a frequency around 19.629 GHz in these experiments, this concept can work at carrier frequencies from 500 MHz to 1 THz because of the broadband nature of the EIT/AT approach [6], [7]. However, the PPWG would need to be re-designed if the frequency is above 37.5 GHz. The PPWG structure is designed to ensure a transverse electromagnetic (TEM) mode propagates in the structure for both the LO and SIG frequencies. The PPWG supports a fundamental TEM mode from DC to a frequency that corresponds to a wavelength of $2h$ (where h is the separation between the two plates). The PPWG shown in Fig. 2 supports a TEM mode up to a frequency of 37.5 GHz.

For the Rydberg atom-based mixer to accurately measure the phase of the SIG, the phase of both the LO and SIG must be stable with respect to one another over the time-period of the measurement. We use two different methods of stabilization depending on the type of measurement being performed. In the first method, we use a RF mixer to synchronize the LO and SIG when detecting the beat note. The oscilloscope is triggered by mixing the LO and SIG using an RF mixer. This will remove any common phase difference between LO and SIG. This first method is suitable when performing measurements in a laboratory where both the SG and VSG can be co-located and connected. The second method uses two rubidium (Rb) clocks to independently synchronize the



(a)



(b)

FIGURE 3. Experimental setup: (a) photo and (b) diagram.

LO and SIG, which is suitable when the LO and SIG are not co-located. These two Rb clocks supply a reference signal to both the SG and VSG separately. We use both these methods in the results that follow. A detail study of the pros-and-cons of these two approach will be the topic of future work.

IV. EXPERIMENTAL RESULTS

In this section we discuss several examples and types of measurements with this embedded sensor. These examples include measuring, (1) the amplitude of E-fields, (2) the phase of a variable phase shifter, (3) the propagation constant of

a plane wave in free space, (4) the phase states of phase-modulated carriers typically used in communication systems, and (5) the polarization sensitivity of the embedded sensor.

A. E-FIELD MEASUREMENTS WITH EIT AND POWER SWEEPS

Fundamental to the operation of the embedded sensor is the ability of the atoms inside the vapor cell to respond to E-fields generated by both the LO and the SIG. To confirm this, the E-field strength inside the vapor cell for these two excitations is measured by the EIT/AT approach [5]–[7].

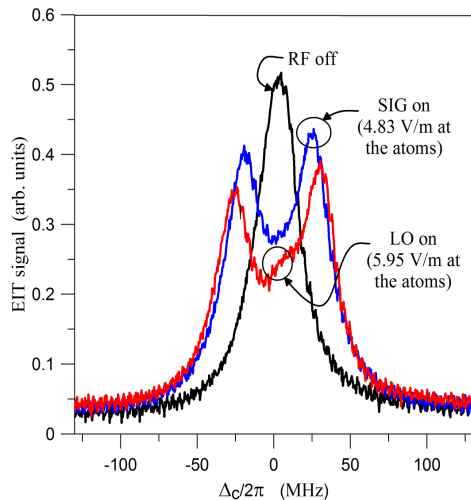


FIGURE 4. The EIT signal measured with the embedded sensor. Shown here is the case with no RF, the case when only the LO SG is on, and the case when only the SIG VSG is on.

Fig. 4 shows the probe transmission through the vapor cell (embedded inside the PPWG antenna as shown in Fig. 2) when a coupling laser is counter-propagating through the vapor cell. To obtain this result, the probe laser power into the vapor cell is $480 \mu\text{W}$, and the coupling laser power is 52 mW . The coupling laser frequency was scanned around the ^{133}Cs $6P_{3/2}$ - $34D_{5/2}$ transition, resulting in an EIT peak (labelled ‘RF off’ in Fig. 4).

As discussed in [5]–[7], applying an RF field caused the EIT signal to split, where the splitting is proportional to the magnitude of the applied RF E-field strength. By measuring the splitting (Δf_m), the magnitude of the applied E-field can be determined by [5]–[7], [19]

$$|E| = 2\pi \frac{\hbar}{\wp} \Delta f_m, \quad (3)$$

where \hbar is Planck’s constant (defined in November 2018 in the re-definition of the SI and went into effect on May 20, 2019 [2] and [3]) and \wp is the atomic dipole moment of the RF transition. We apply an RF field at 19.629230 GHz to couple states $34D_{5/2}$ and $35P_{3/2}$. A typical AT splitting signal obtained by driving the embedded sensor with the LO is shown in Fig. 4 (labelled ‘LO on’). This corresponds to an RF power of -19.7 dBm (measured at the coaxial adapter at the input of the PPWG antenna). An AT splitting signal is also obtained by applying a $f_{\text{SIG}} = 19.629000 \text{ GHz}$ field using a horn antenna placed 348 mm away from the PPWG antenna (labelled ‘SIG on’ in Fig. 4). This corresponds to a SIG RF power of -6.1 dBm (measured at the input to the horn antenna). These results illustrate that the embedded sensor can effectively capture RF E-fields from external sources.

Also shown in Fig. 4 is the calculated E-field strength from (3), which requires a calculated value of \wp . Calculating \wp involves a numerical solution to the Schrödinger equation for the atomic wavefunctions, and then a numerical evaluation of the radial overlap integrals involving the

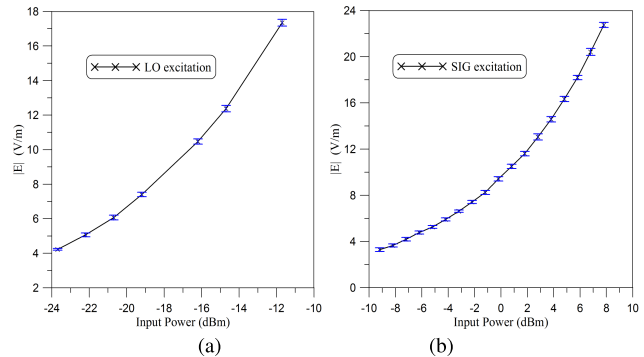


FIGURE 5. The measured E-field with the embedded sensor as a function of input power. The power level corresponds to input power to the parallel-plate antenna (for the LO case) or the input power to the horn antenna (for SIG case): (a) LO and (b) SIG. The error bars represent the standard deviation of ten measurements.

wavefunctions for a set of atomic states [1] and [6]. For a given atomic state, these numerical calculations require one to use the quantum defects (along with the Rydberg formula [1]) for the ^{133}Cs [34]–[36]. For this measurement, the dipole moment for the resonant RF transition is calculated to be $\wp = 723.4 ea_0$ (which includes a radial part of $1476.6 ea_0$ and an angular part of 0.48989 , which correspond to co-linear polarized optical and RF fields, where e is the elementary charge and a_0 is the Bohr radius: $a_0 = 0.529177 \times 10^{-10} \text{ m}$).

Fig. 5 shows the measured E-field for different input power levels for the two different source excitations (for both the LO and from the SIG generated from the horn antenna). The results in this figure are obtained by measuring Δf_m and using (3). The power levels on the x-axis of the plot correspond to the input power to the parallel-plate antenna (for the LO case) or the input power to the horn antenna (for SIG case). The results in Figs. 4 and 5 illustrate that the embedded sensor can effectively respond to E-fields generated by either the LO or the SIG. The errors and uncertainties of these types of measurements are related to the EIT/AT detection scheme in general and are discussed in [32].

As stated above, RF standing waves do exist inside the vapor cell [7], [8], [31]. Here the measurements represent the field strength at the atoms, including the effect of the vapor cell walls and standing waves. Since during the experiments, the laser positions are fixed at a location inside the vapor cell, these standing wave effects will not affect the phase and relative amplitude measurements presented here.

B. BEAT NOTE SIGNAL FROM THE MIXER

As shown in [25], the amplitude of the beat note is a function of the LO and SIG E-field strength. Fig. 6 shows the beat note signal for the embedded sensor measurement from the photodetector for $f_{\text{LO}} = 19.629230 \text{ GHz}$ and $f_{\text{SIG}} = 19.629000 \text{ GHz}$ (or $f_{\text{IF}} = 230 \text{ kHz}$). This data is for a given LO strength and different SIG strengths. The measured data clearly show the 230 kHz cosine behavior of the beat note signal as a function of time. In a later section, we use the

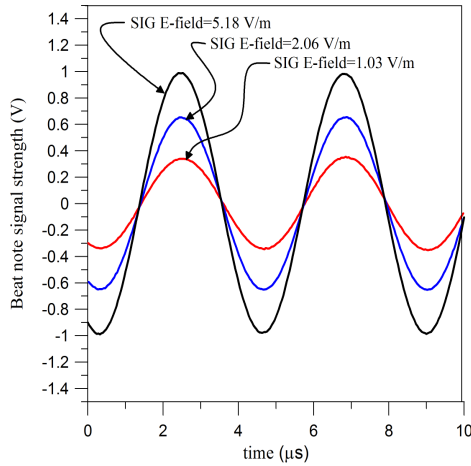


FIGURE 6. The beat note signal measured on the oscilloscope. These data are for an LO field of 6.14 V/m and three different SIG field levels, with frequencies $f_{LO} = 19.629230$ GHz and $f_{SIG} = 19.629000$ GHz (for an $f_F = 230$ kHz). Each curve corresponds to 5 averages.

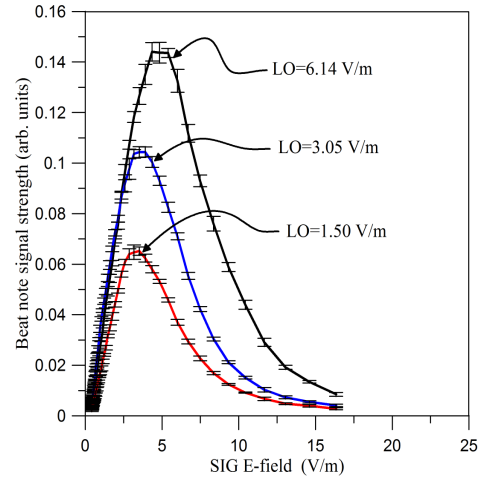
relative amplitude of the beat note to investigate the polarization sensitivity of the embedded sensor.

The beat note amplitude is a non-linear function of the E-field for both the LO and SIG, where the E-field strength seen by the atoms is given by [28]

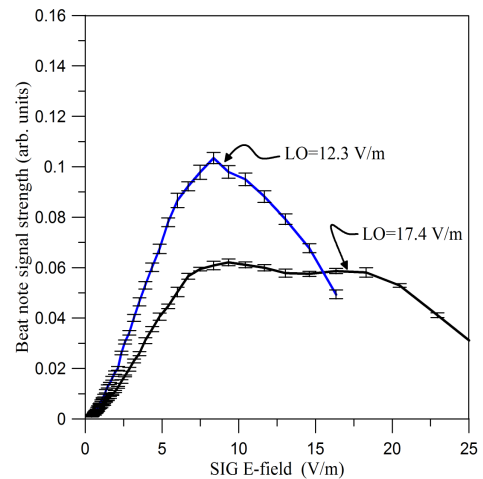
$$|E_{atoms}| = \sqrt{E_{LO}^2 + E_{SIG}^2 + 2E_{LO}E_{SIG}\cos(2\pi f_{IF}t + \Delta\phi)} \tag{4}$$

where E_{LO} and E_{SIG} are the E-field strengths of the LO and SIG, respectively. Fig. 7 shows a family of curves for the beat note amplitude obtained for the embedded sensor. Here we use an RF mixer for LO and SIG synchronization.

There is a minimum RF field level that is required before the splitting shown in Fig. 4 occurs. When an RF-field strength is increased from zero, the amplitude of the EIT signal decreases and its linewidth broadens before the EIT signal splits into two peaks [5]. Fig. 7a corresponds to the situation where the E-field strength for the LO is weak enough such that splitting does not occur. From this figure, we see the beat note strength has a maximum for a given ratio of LO and SIG field strengths. When the strength of the LO and SIG are such that AT splitting occurs, the probe laser must be frequency tuned to be on-resonance with a split AT peak. As the LO or SIG field strength increases further, the probe laser frequency must be further tuned to maintain resonance with an AT peak for maximum beat note signal strength. The results of the beat note under this situation is shown in Fig. 7(b). In Fig. 7(a) the lasers are locked to the maximum of the EIT peak, while in Fig. 7(b) the field strengths are such that the EIT signal splits, and the probe laser frequency was tuned to one of the AT peaks. The error bars on Fig. 7 represent the standard deviation from five sets of experiments, indicating good repeatability of the measurement. The errors and uncertainties associated with these measurements are mainly due to laser power and laser frequency stability.



(a)



(b)

FIGURE 7. The amplitude of the beat-note signal as a function of field strength for both the LO and SIG signal. These data are for $f_{LO} = 19.629230$ GHz and $f_{SIG} = 19.629000$ GHz (or $f_F = 230$ kHz): (a) no AT splitting on the EIT signal and (b) AT splitting on the EIT signal. The error bars represent the standard deviation of five measurements.

As one might expect, the results in this figure show that for a given LO field strength, there is an optimal SIG field strength to obtain the largest beat note amplitude. This is especially true when operating in the non-AT-splitting situation (i.e., $\Delta_c = 0$). When operating in the AT-splitting situation, one can track an AT peak using the probe laser frequency to find the maximum beat note amplitude. When the AT peaks split such that there is no overlap between the AT peaks at zero coupling laser detuning (the center of Fig. 4), the maximum beat note is found when the probe laser is tuned to the side of the AT peak, rather than the top of the peak. Note in Fig. 7(b) that the ‘LO = 17.4 V/m’ trace has two maxima - one for the probe laser frequency on one side of the AT peak, and a second for when the SIG field strength further splits the AT peaks such that the probe laser frequency is on the other side of the AT peak. There is a slight dip in beat note signal strength when the probe laser frequency sits on the top of the AT peak.

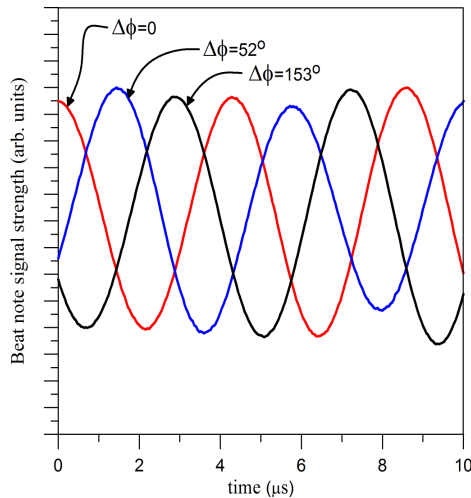


FIGURE 8. The measured beat note on the oscilloscope for different phase shifts of the SIG field, for $f_{LO} = 19.629230$ GHz and $f_{SIG} = 19.629000$ GHz ($f_{IF} = 230$ kHz). Each curve corresponds to 5 averages.

One advantage of having the vapor cell embedded inside the PPWG antenna (as opposed to having the LO and SIG transmitted from the same location as was done in [25] and [29]) is that it allows one to easily change the LO field at the atoms by varying the input power to the PPWG antenna. That is, the embedded sensor head allows one to easily vary the LO E-field to find the optimal value for the LO/SIG ratio in order to maximize the beat note signal strength.

C. MEASURING THE PHASE OF A VARIABLE PHASE SHIFTER

Here we show the ability of the atom-based embedded sensor to measure the phase of an RF field by using the sensor to measure the phase shift introduced by a variable phase shifter. For this set of data, we use the same experimental setup shown in Fig. 3, with the exception that a variable phase shifter was placed between the VSG and the horn antenna. This allows us to vary the phase of the SIG that is feeding the horn antenna. For various settings on the variable phase shifter, the phase shift (relative to the RF mixer-synchronized signal) was measured with the embedded sensor. For each setting, the variable phase shifter was removed from the experimental setup and connected to a vector network analyzer (VNA) such that the phase shift introduced by the variable phase shifter can be measured independently.

Fig. 8 shows the beat note measured on the photodetector for three different phase shifts of the SIG field. The cosine variation of the beat note is clearly observed in this figure. Fig. 9 shows the phase measured with the embedded sensor versus the phase measured with the VNA, similar data is shown in [37]. Also plotted is a line representing $\Delta\phi_{\text{mixer}} = \Delta\phi_{\text{VNA}}$. We see that the data falls along this line, indicating a one-to-one correspondence between the two measured phase values, i.e., the phase obtained from the embedded sensor is the same as the phase measured with the VNA. The error bars

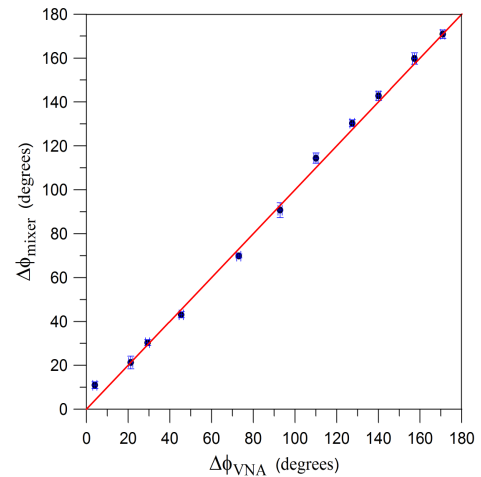


FIGURE 9. The measured phase of the variable phase shifter, for $f_{LO} = 19.629230$ GHz and $f_{SIG} = 19.629000$ GHz ($f_{IF} = 230$ kHz).

in the data correspond to performing five separate measurements, illustrating the repeatability of the measurement. Notice that each phase measurement is fairly precise, in that the error bars are small. The standard deviation indicates that the phase is measured to within 2° . However, data from each phase measurement do not lie exactly on the line. This is due to that fact that the variable phase shifter was disconnected from the experimental setup each setting and measured on the VNA. The act of connecting and disconnecting the phase shifter results in a small phase change due to the connectors (repeatability of the act of connecting and disconnecting the device). With that said, we see that the embedded sensor does an excellent job of measuring phase when compared to the VNA measurements.

D. MEASURING THE PROPAGATION CONSTANT OF FREE SPACE

The propagation constant for a 19.629000 GHz wave in free space is measured with the embedded sensor. We use the same experimental setup shown in Fig. 3, with the exception that the horn antenna is placed on a translation stage such that the horn antenna could be placed at different distances from the embedded sensor. The phase of a 19.629000 GHz CW SIG at various locations of the horn antenna is measured with the embedded sensor for $f_{LO} = 19.629230$ GHz (where $f_{IF} = 230$ kHz). Fig. 10 shows the measured phase change ($\Delta\phi$) versus the change in the location of the horn antenna (Δd). Also shown in this figure are the error bars representing the standard deviation for ten data runs. The slope of the data is the propagation constant of free space ($\beta_{\text{measured}} = \Delta\phi / \Delta d$) and is determined to be $\beta_{\text{measured}} = 408.8$ rad/s (also shown in the figure). The theoretical value is $\beta_{\text{theory}} = 2\pi f_{SIG} / c = 411.1$ rad/s (also shown in the figure), where c is the speed of light in *vacuo*. The percent difference in the measured and theoretical values of β is 0.6%. In this case our errors are mainly due to uncertainty in the positioning and alignment of the SIG horn.

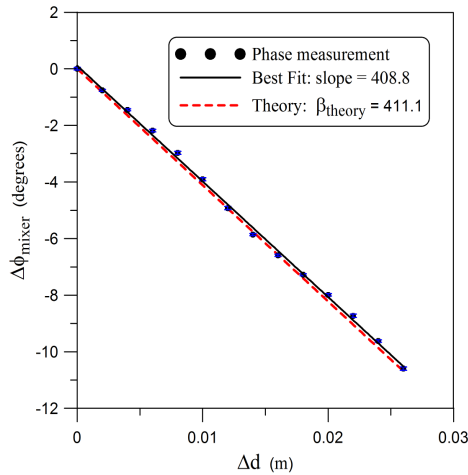


FIGURE 10. The measured propagation constant ($\Delta\phi/\Delta d$), for $f_{LO} = 19.629230$ GHz and $f_{SIG} = 19.629000$ GHz ($f_{IF} = 230$ kHz).

E. DETECTING PHASE MODULATED CARRIER SIGNAL

A real-world application of this embedded atomic sensor is as a communications receiver. In principle, the Rydberg atom-based RF sensor can be used to detect RF signals on carriers from 500 MHz up to 1 THz, making them a promising candidate for future high-frequency communications. Here, we show results for detecting phase-modulated carriers by transmitting BPSK (binary phase shift keying) and QPSK (quadrature phase shift keying) modulated signals and receiving them with the embedded Rydberg atom sensor. In BPSK and QPSK, information (bits) are encoded onto a CW carrier by changing the phase of the CW carrier in a given symbol. For example, BPSK uses two different phase states to transmit data, in which the carrier frequency phase is changed between 0° and 180° . Each phase state represents one transmitted symbol and each symbol is mapped into bits “1” or “0”. In QPSK, each transmitted symbol (or phase state) is mapped into two bits. This is done by choosing one of four possible phases applied to a CW carrier: 45° (binary state “00”), 135° (binary state “01”), -45° (binary state “10”), and -135° (binary state “11”). To demonstrate the reception of BPSK and QPSK with the embedded sensor, we use the same experimental setup shown in Fig. 3, with the exception that the oscilloscope is replaced with a vector signal analyzer (VSA). The VSA can detect the phase state of a down-converted signal and hence recover the phase-state of the modulated carrier. For these measurements, the LO and SIG were synchronized with Rb clocks.

An in-phase and quadrature (IQ) constellation diagram is typically used to represent the phase states for a large number of transmitted symbols. Fig. 11(a) shows the constellation diagram received with the embedded sensor for a BPSK modulation scheme for a stream of 2047 symbols. For these results we used $f_{LO} = 19.6290$ GHz and $f_{SIG} = 19.6295$ GHz (or $f_{IF} = 500$ kHz). The scatter plot on the right side of Fig. 11(a) corresponds to the reception of a phase state of 0° (or a binary state of 1), and the scatter plot of the left

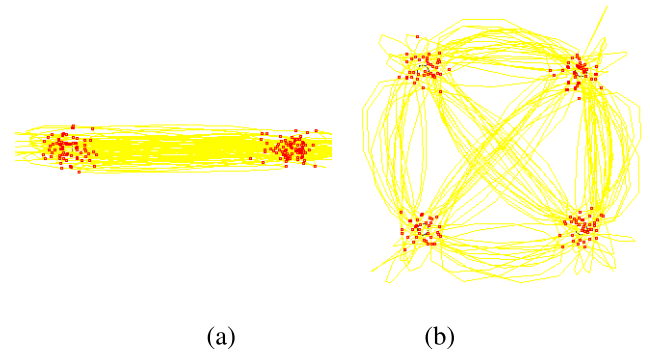


FIGURE 11. The receiver constellation diagram for a 2047 symbol stream. These data are for $f_{LO} = 19.6290$ GHz and $f_{SIG} = 19.6295$ GHz (or $f_{IF} = 500$ kHz): (a) BPSK and (b) QPSK.

correspond to the reception of a phase state of 180° (or a binary state of 0).

Fig. 11(b) shows the constellation diagrams for a QPSK modulation scheme for a stream of 2047 symbols. The grouping of the data in the four quadrants correspond to the reception of four possible phase states (45° : binary state “00”, 135° : binary state “01”, -45° : binary state “10”, and -135° : binary state “11”). These results show that the embedded sensor can detect and receive typical phase modulated carrier signals used in conventional communication systems. One of the advantages of the Rydberg atom-based receiver is that the atoms automatically down-convert the SIG modulated carrier to the IF (and convert it to an optical signal as the amplitude of the probe laser transmission) without any conventional down-conversion electronics.

F. POLARIZATION DETECTION AND SENSITIVITY

The embedded sensor has an inherent polarization selectivity feature due to the geometry of the PPWG antenna. The PPWG antenna (and hence the embedded sensor head) is more sensitive to an x -polarization E-field [where the x -axis points from one plate to the other, see Fig. 3(b)] and rejects E-field polarized in the y -direction [where the y -axis points along the axis of the lasers, see Fig. 3(b)]. In this PPWG structure, the vapor cell always sees an x -polarized RF field, so the RF field is always co-polarized with the laser fields at the atoms. Fig. 12 shows the measurement of the relative E-field obtained with the embedded sensor for a transmitting horn antenna rotated relative to the x -axis (i.e., a x -polarized E-field to a y -polarized E-field). The bottom axis of the plot corresponds to the angle of the horn antenna relative to PPWG antenna, where an angle of 0° corresponds to the antenna horn and the parallel-plate antenna being co-polarized (i.e., both polarized in the x -direction) and a degree of 90° corresponds to the cross-polarized case (the antenna horn polarized along the y -axis). Also shown in this figure are the error bars for ten set of data, which indicate that the E-field is measured to within 1 % for this case.

The results in this figure show two different methods for determining the E-field. The dash curve are results obtained

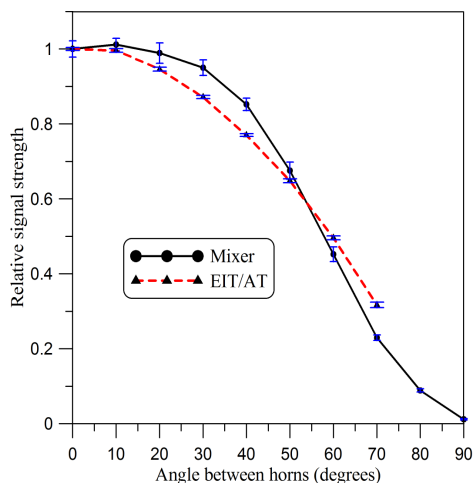


FIGURE 12. Polarization sensitivity: The relative field strength as the horn antenna is rotated from the x -axis to the y -axis, for $f_{LO} = 19.629230$ GHz and $f_{SIG} = 19.629000$ GHz (or $f_{IF} = 230$ kHz). The horn antenna is placed 358 mm from the embedded sensor head.

from measuring the EIT/AT splitting [i.e., eq. (3)]. The solid curves correspond to the results using the beat note amplitude obtained using the atom mixer, as discussed in [28]. The amplitude of the beat note signal decreases as the horn antenna is rotated from the x -axis to the y -axis. Note the two approaches have different dependence on the angle. The measured AT-split is dependent on the strength of the incident RF field that enters the PPWG, which follows a cosine dependence on the angle between the antennas. While in the case of the mixer, the strength of the beat note signal is a more involved function of the strength of the incident RF field (4). This comparison shows the polarization selectivity of the embedded sensor/atom system. The results also show that the mixer method for determining the E-field can measure a much smaller E-field strength than that using the EIT/AT method. Note that the EIT/AT cannot detect a E-field below $\sim 80\%$ of the peak value. The ability of the mixer to measure weak E-field strengths is also discussed in [28]. The error bars in Fig. 12 correspond to the standard deviation of 10 data sets, indicating the repeatability of the technique. Here the errors are again mainly due to uncertainty in the positioning and alignment of the SIG horn.

We should emphasize that the results in Fig. 12 are a relative field measurement as a function of angle. While the EIT/AT method can be used to obtain absolute E-field measurements, the mixer approach requires an additional calibration. As discussed in [28], the EIT/AT approach can be used to calibrate the mixer approach.

V. DISCUSSION AND CONCLUSION

We have introduced a Rydberg atom-based embedded sensor, which consists of an atomic vapor cell embedded in a parallel plate waveguide antenna. This atomic embedded sensor allows for the measurement and detection of both the amplitude and phase of an RF CW field as well as modulated

signals. We show several examples illustrating the capability of this embedded sensor. The results presented here demonstrate that this embedded atomic sensor gives us the ability to measure the magnitude, phase, and discriminate polarization of an RF field, all in one compact quantum-based sensor head. By embedding the atom system in a waveguide to apply an LO (this combined system has not been done before), we are able to control the RF LO field at the atoms, which allows us to control the properties of the atom-based mixer and maximize the ability to measure phase and amplitude of the field or receive a modulated signal.

Rydberg atom-based sensors can be used in two distinct ways: either to perform direct calibrated measurements, as was the intent of the original work [4]–[7], or as receivers, where absolute field values may not be required. If one is interested in a non-invasive sensor that would have minimal influence on the E-field (i.e., for use as direct calibrated measurement), an embedded sensor would not be the best choice, as the metal of the PPWG does perturb the field being measured and the PPWG embedded sensor introduces an additional calibration step for absolute field measurements as compared with a bare vapor cell [4]–[7]. Whereas, an embedded sensor is a good choice for receiver applications.

There are various aspects of the embedded sensor, and Rydberg atom-based sensors in general, that should be discussed. Rydberg atom-based receivers are inherently different from the electronic components in the front-end of traditional RF receivers. As such, different performance metrics may be needed to compare these two systems. These performance metrics and the pros-and-cons of the Rydberg-atom system compared to a traditional system are currently being investigated. However, we can make a few preliminary observations concerning some of the aspects of Rydberg atom-based systems. Rydberg atom-based receivers and sensors have potential advantages over conventional radio technologies, which include: (1) micron-size sensors over a frequency range of 500 MHz to 1 THz [6], [7], (2) multi-band (or multi-channel) operation in one compact vapor cell [27], [38], (3) the possibility of being less susceptible to noise [24] and [27], (4) ultra-high sensitivity reception from 500 MHz to 1 THz [28] with sub Hz frequency resolution, and (5) no need for traditional down-conversion electronics because the atoms automatically down-convert the phase modulated signals to an IF. Furthermore, the Rydberg atom-based receiver has the possibility of being less affected by “spoofing” and “jamming” (as well as noise) when compared to conventional systems. The atom-based receiver interacts with noise in a different manner than conventional systems and as such may be less susceptible to noise. This is indicated in [24], [27], where E-field strengths and modulated signals could be measured and detected in the presence of band-limited white Gaussian noise for low CW-signal to noise-power ratio conditions. While the bandwidth of these Rydberg-atom receivers/sensors depend on the Rydberg state chosen, in general, the bandwidth is limited by the response time of the atomic transition, which is on the order of 10 MHz

[29], [39], and [40]. Finally, in order for these Rydberg atom-based sensors to become commercially available, technologies will need to be developed. One of the key needed technologies are compact and inexpensive coupling lasers, which are currently being investigated by a few commercial companies. With that said, the potential benefits of the Rydberg-atom systems have spawned a growing interest in the field and several companies are currently investigating these needed technologies. These potential advantages make it worthwhile to explore the capabilities and potential applications of the Rydberg atom-based receivers.

While the experimental setup used in this paper is performed on the optical table, the embedded atomic sensor can be designed to be fiber-coupled such that measurements are not confined to the optical table (similar to what was presented in [23]). This will be the topic of future work. Finally, while we demonstrated a Rydberg atom-based sensor embedded in a PPWG, we note that the atomic vapor cell can be integrated inside other waveguiding and antenna structures for an array of other applications.

REFERENCES

- [1] T. F. Gallagher, *Rydberg Atoms*. Cambridge, U.K.: Cambridge Univ. Press, 1994.
- [2] M. Stock, "The revision of the SI—towards an international system of units based on defining constants," *Meas. Techn.*, vol. 60, no. 12, pp. 1169–1177, 2018.
- [3] *Road to Revised SI*. Accessed: 2018. [Online]. Available: <https://www.nist.gov/si-redefinition/road-revised-si>
- [4] J. A. Gordon, C. L. Holloway, S. Jefferts, and T. Heavner, "Quantum-based SI traceable electric-field probe," in *Proc. IEEE Int. Symp. Electromagn. Compat.*, Jul. 2010, pp. 321–324.
- [5] J. A. Sedlacek, A. Schwettmann, H. Kübler, R. Löw, T. Pfau, and J. P. Shaffer, "Microwave electrometry with Rydberg atoms in a vapour cell using bright atomic resonances," *Nature Phys.*, vol. 8, no. 11, p. 819, 2012.
- [6] C. L. Holloway, J. A. Gordon, A. Schwarzkopf, D. A. Anderson, S. A. Miller, N. Thaicharoen, and G. Raithel, "Broadband Rydberg atom-based electric-field probe for SI-traceable, self-calibrated measurements," *IEEE Trans. Antenna Propag.*, vol. 62, no. 12, pp. 6169–6182, Dec. 2014.
- [7] C. L. Holloway, M. T. Simons, J. A. Gordon, P. F. Wilson, C. M. Cooke, D. A. Anderson, and G. Raithel, "Atom-based RF electric field metrology: From self-calibrated measurements to subwavelength and near-field imaging," *IEEE Trans. Electromagn. Compat.*, vol. 59, no. 2, pp. 717–728, Apr. 2017.
- [8] C. L. Holloway, J. A. Gordon, A. Schwarzkopf, D. A. Anderson, S. A. Miller, N. Thaicharoen, and G. Raithel, "Sub-wavelength imaging and field mapping via electromagnetically induced transparency and Autler-Townes splitting in Rydberg atoms," *Appl. Phys. Lett.*, vol. 104, pp. 244102-1–244102-5, Jun. 2014.
- [9] J. A. Sedlacek, A. Schwettmann, H. Kübler, and J. P. Shaffer, "Atom-based vector microwave electrometry using rubidium Rydberg atoms in a vapor cell," *Phys. Rev. Lett.*, vol. 111, Aug. 2013, Art. no. 063001.
- [10] J. A. Gordon, C. L. Holloway, A. Schwarzkopf, D. A. Anderson, S. Miller, N. Thaicharoen, and G. Raithel, "Millimeter wave detection via Autler-Townes splitting in rubidium Rydberg atoms," *Appl. Phys. Lett.*, vol. 105, Jul. 2014, Art. no. 024104.
- [11] H. Fan, S. Kumar, J. Sedlacek, H. Kubler, S. Karimkashi, and J. P. Shaffer, "Atom based RF electric field sensing," *J. Phys. B, At. Mol. Opt. Phys.*, vol. 48, no. 20, 2015, Art. no. 202001.
- [12] M. Tanasittikosol, J. D. Pritchard, D. Maxwell, A. Gauguet, K. J. Weatherill, R. M. Potvliege, and C. S. Adams, "Microwave dressing of Rydberg dark states," *J. Phys. B, At. Mol. Opt. Phys.*, vol. 44, no. 18, 2011, Art. no. 184020.
- [13] C. G. Wade, N. Šibalić, N. R. de Melo, J. M. Kondo, C. S. Adams, and K. J. Weatherill, "Real-time near-field terahertz imaging with atomic optical fluorescence," *Nature Photon.*, vol. 11, no. 1, pp. 40–43, 2017.
- [14] S. Kumar, H. Fan, H. Kübler, J. Sheng, and J. P. Shaffer, "Atom-based sensing of weak radio frequency electric fields using homodyne readout," *Sci. Rep.*, vol. 7, Feb. 2019, Art. no. 42981.
- [15] D. A. Anderson, E. G. Paradis, and G. Raithel, "A vapor-cell atomic sensor for radio-frequency field detection using a polarization-selective field enhancement resonator," *Appl. Phys. Lett.*, vol. 113, no. 7, 2018, Art. no. 073501.
- [16] D. A. Anderson, S. A. Miller, G. Raithel, J. A. Gordon, M. L. Butler, and C. L. Holloway, "Optical measurements of strong microwave fields with Rydberg atoms in a vapor cell," *Phys. Rev. Appl.*, vol. 5, Mar. 2016, Art. no. 034003.
- [17] D. A. Anderson, S. A. Miller, A. Schwarzkopf, C. L. Holloway, J. A. Gordon, N. Thaicharoen, and G. Raithel, "Two-photon microwave transitions and strong-field effects in a room-temperature Rydberg-atom gas," *Phys. Rev. A, Gen. Phys.*, vol. 90, no. 4, 2014, Art. no. 043419.
- [18] A. K. Mohapatra, T. R. Jackson, and C. S. Adams, "Coherent optical detection of highly excited Rydberg states using electromagnetically induced transparency," *Phys. Rev. Lett.*, vol. 98, no. 11, 2007, Art. no. 113003.
- [19] C. L. Holloway, M. T. Simons, J. A. Gordon, A. Dienstfrey, D. A. Anderson, and G. Raithel, "Electric field metrology for SI traceability: Systematic measurement uncertainties in electromagnetically induced transparency in atomic vapor," *J. Appl. Phys.*, vol. 121, May 2017, pp. 233106-1–233106-9.
- [20] M. T. Simons, J. A. Gordon, and C. L. Holloway, D. A. Anderson, S. A. Miller, and G. Raithel, "Using frequency detuning to improve the sensitivity of electric field measurements via electromagnetically induced transparency and Autler-Townes splitting in Rydberg atoms," *Appl. Phys. Lett.*, vol. 108, Mar. 2016, Art. no. 174101.
- [21] M. T. Simons, J. A. Gordon, and C. L. Holloway, "Simultaneous use of Cs and Rb Rydberg atoms for dipole moment assessment and RF electric field measurements via electromagnetically induced transparency," *J. Appl. Phys.*, vol. 102, no. 12, 2016, Art. no. 123103.
- [22] C. L. Holloway, M. T. Simons, M. D. Kautz, A. H. Haddab, J. A. Gordon, and T. P. Crowley, "A quantum-based power standard: Using Rydberg atoms for a SI-traceable radio-frequency power measurement technique in rectangular waveguides," *Appl. Phys. Lett.*, vol. 113, Aug. 2018, Art. no. 094101.
- [23] M. T. Simons, J. A. Gordon, and C. L. Holloway, "Fiber-coupled vapor cell for a portable Rydberg atom-based radio frequency electric field sensor," *Appl. Opt.*, vol. 57, no. 22, pp. 6456–6460, 2018.
- [24] M. T. Simons, M. D. Kautz, C. L. Holloway, D. A. Anderson, G. Raithel, D. Stack, M. C. S. John, and W. Su, "Electromagnetically induced transparency (EIT) and Autler-Townes (AT) splitting in the presence of band-limited white Gaussian noise," *J. Appl. Phys.*, vol. 123, no. 20, 2018, Art. no. 203105.
- [25] M. T. Simons, A. H. Haddab, J. A. Gordon, and C. L. Holloway, "A Rydberg atom-based mixer: Measuring the phase of a radio frequency wave," *Appl. Phys. Lett.*, vol. 114, no. 11, 2019, Art. no. 114101.
- [26] L. J. Chu, "Physical limitations of omni-directional antennas," *J. Appl. Phys.*, vol. 19, no. 12, p. 1163, 1948.
- [27] C. L. Holloway, M. T. Simons, A. H. Haddab, J. A. Gordon, and S. Voran, "A multiple-band Rydberg-atom based receiver/antenna: AM/FM stereo reception," *IEEE Antennas Propag. Mag.*, to be published.
- [28] J. A. Gordon, M. T. Simons, A. H. Haddab, and C. L. Holloway, "Weak electric-field detection with sub-1 Hz resolution at radio frequencies using a Rydberg atom-based mixer," *AIP Adv.*, vol. 9, no. 4, 2019, Art. no. 045030.
- [29] C. L. Holloway, M. T. Simons, A. H. Haddab, J. A. Gordon, and D. Novonty, "Detecting and receiving phase-modulated signals with a Rydberg atom-based mixer," *IEEE Antennas Wireless Propag. Lett.*, vol. 18, no. 9, pp. 1853–1857, Sep. 2019.
- [30] D. Barredo, H. Kübler, R. Daschner, R. Löw, and T. Pfau, "Electrical readout for coherent phenomena involving Rydberg atoms in thermal vapor cells," *Phys. Rev. Lett.*, vol. 110, Mar. 2013, Art. no. 123022.
- [31] H. Fan, S. Kumar, J. Sheng, J. P. Shaffer, C. L. Holloway, and J. A. Gordon, "Effect of vapor cell geometry on Rydberg atom-based radio-frequency electric field measurements," *Phys. Rev. Appl.*, vol. 4, Nov. 2015, Art. no. 044015.
- [32] M. T. Simons, M. Kautz, J. A. Gordon, and C. L. Holloway, "Uncertainties in Rydberg atom-based RF E-field measurements," in *Proc. EMC Eur.*, Amsterdam, The Netherlands, Aug. 2018, pp. 376–380.
- [33] D. A. Steck. (Dec. 23, 2010). *Cesium D Line Data Revision 2.1.4*. [Online]. Available: <http://steck.us/alkalidata>

- [34] P. Goy, J. M. Raimond, G. Vitrant, and S. Haroche, "Millimeter-wave spectroscopy in cesium Rydberg states. Quantum defects, fine- and hyperfine-structure measurements," *Phys. Rev. A, Gen. Phys.*, vol. 26, no. 5, pp. 2733–2742, Nov. 1982.
- [35] K.-H. Weber and C. J. Sansonetti, "Accurate energies of nS, nP, nD, nF, and nG levels of neutral cesium," *Phys. Rev. A, Gen. Phys.*, vol. 35, no. 11, pp. 4650–4660, Jun. 1987.
- [36] J. Deiglmayr, H. Herburger, H. Saßmannshausen, P. Jansen, H. Schmutz, and F. Merkt, "Precision measurement of the ionization energy of Cs," *Phys. Rev. A, Gen. Phys.*, vol. 93, no. 1, 2016, Art. no. 013424.
- [37] M. T. Simons, A. H. Haddab, J. A. Gordon, and C. L. Holloway, "Applications with a Rydberg atom-based radio frequency antenna/receiver," in *Proc. EMC Eur.*, Barcelona, Spain, Sep. 2019, pp. 885–889.
- [38] D. A. Anderson, R. E. Sapiro, and G. Raithel, "An atomic receiver for AM and FM radio communication," Aug. 2018, *arXiv:1808.08589v1*. [Online]. Available: <https://arxiv.org/abs/1808.08589v1>
- [39] Z. Song, W. Zhang, H. Liu, X. Liu, H. Zhou, J. Zhang, and J. Qu, "Rydberg-atom-based digital communication using a continuously tunable radio-frequency carrier," *Opt. Express*, vol. 27, no. 6, pp. 8848–8857, 2019.
- [40] A. B. Deb and N. Kjergaard, "Radio-over-fiber using an optical antenna based on Rydberg states of atoms," *Appl. Phys. Lett.*, vol. 112, no. 21, 2018, Art. no. 211106.



JOSHUA A. GORDON (M'05–SM'16) received the Ph.D. degree in optics and electromagnetics from the College of Optical Sciences, University of Arizona, Tucson, AZ, USA. He is currently a Physicist with the Electromagnetics Division, NIST. His current research areas investigate new technologies for electric field measurements, which include robotic based antenna metrology systems, optical techniques for antenna alignment, and atom-based electric-field sensing.



DAVID NOVOTNY received the B.Sc. degree in electrical engineering from the University of Colorado, in 1990, and the M.Sc. degree in electrical engineering from the University of Colorado, in 1996. He joined the National Institute of Standards and Technology's Electromagnetics Division. He has worked on EMC facility evaluations using broadband synthetic time-domain analysis, which has been used to evaluate EM shielding of many facilities and airframes, including E-3, an E-10 prototype configuration, several commercial aircraft, and the Space Shuttle Endeavour. Since 2000, he has been working in antenna metrology, designing systems and methods for accurate measurements of antenna parameters. He was a part of teams that designed speciality systems to exercise and exploit electronic identity and travel documents, image EM facilities for non-ideal reflections, generate standard EM fields for device testing, and using robots to perform complex EM and antenna measurements.



CHRISTOPHER L. HOLLOWAY (S'86–M'92–SM'04–F'10) received the B.S. degree in engineering from the University of Tennessee at Chattanooga, Chattanooga, TN, USA, and the M.S. and Ph.D. degrees from the University of Colorado at Boulder, Boulder, CO, USA. During 1992, he was a Research Scientist with Electro Magnetic Applications, Inc., Lakewood, CO, USA. His responsibilities included theoretical analysis and finite-difference time-domain modeling of various electromagnetic problems. From 1992 to 1994, he was with the National Center for Atmospheric Research (NCAR), Boulder, CO, USA. While at NCAR, his duties included wave propagation modeling, signal processing studies, and radar systems design. From 1994 to 2000, he was with the Institute for Telecommunication Sciences, U.S. Department of Commerce, Boulder, CO, USA, where he was involved in wave propagation studies. Since 2000, he has been with the National Institute of Standards and Technology, Boulder, CO, USA, where he works on electromagnetic theory and measurements, quantum optics, and atom-based metrology. He is a member of the URSI Commissions A, B, and E. He worked as the Chair of the U.S. Commission A of URSI, from 2012 to 2015, and an Associate Editor of the IEEE TRANSACTIONS ON ELECTROMAGNETIC COMPATIBILITY, from 1998 to 2018. He was the Chairman of the Technical Committee on Computational Electromagnetics (TC-9) of the IEEE Electromagnetic Compatibility Society, from 2000 to 2005, the Co-Chair of the Technical Committee on Nano-Technology and Advanced Materials (TC-11) of the IEEE Electromagnetic Compatibility Society, from 2006 to 2011, and the IEEE Distinguished Lecturer for the Electromagnetic Compatibility Society, from 2004 to 2006.

• • •



MATTHEW T. SIMONS (M'16) received the B.S. degree in physics from the University of Virginia, Charlottesville, VA, USA, in 2007, and the M.S. and Ph.D. degrees in physics from the College of William and Mary, Williamsburg, VA, USA, in 2009 and 2014, respectively. Since graduating in 2014, he has been a Postdoctoral Researcher as a part of the University of Colorado PREP Program with the RF Technology Division of the Communications Technology Laboratory,

National Institute of Standards and Technology, Boulder, CO, USA, investigating resonant interactions with Rydberg atoms for RF field detection and metrology. His current research interests include in laser-atom interactions, quantum optics, and applying atomic and optical physics to problems in RF, mm-wave, and THz technology.



ABDULAZIZ H. HADDAB (S'17) received the B.S. degree (Hons.) in electrical engineering from Kuwait University, Kuwait City, Kuwait, in 2006, and the M.S. degree in electrical engineering from the University of Colorado at Boulder, Boulder, CO, USA, in 2011, where he is currently pursuing the Ph.D. degree with the Electromagnetics Group. From 2012 to 2015, he was a Faculty Member with the Electrical Engineering Technology Department, Public Authority for Applied Educa-

tion and Training, Kuwait City. He is currently a Research Associate with the National Institute of Standards and Technology (NIST), Boulder, CO, USA, where he has been involved in atom-based metrology. His current research interests include electromagnetic field theory, wave propagation, guided wave structures, and metamaterials. He is an Associate Member of the U.S. National Committee for International Union of Radio Science (USNC-URSI) Commission B.